J. Fluid Mech. (2009), *vol.* 625, *pp.* 299–320.
doi:10.1017/S0022112008005570 Printed in the United Kingdom

Particle capture in binary solidification

JUSTIN C. T. KAO†, ALEXANDER A. GOLOVIN‡, AND STEPHEN H. DAVIS

Department of Engineering Sciences and Applied Mathematics, Northwestern University, Evanston, IL, USA

(Received 5 June 2008 and in revised form 8 December 2008)

We examine the interaction of a spherical foreign particle with a propagating solidification front in a binary alloy. Depending on the material properties and the speed of the front, the particle may be pushed ahead of the front, or engulfed and incorporated into the solid phase. We apply numerical boundary integral and continuation methods to determine the critical speed for particle capture, as a function of the system parameters. We reconcile the differing predictions of previous theoretical works, and show that many typical systems may obey a new scaling of the critical speed, as obtained here. We show that due to constitutional undercooling, the presence of solute decreases particle speeds by an order of magnitude below those for a single-component system. We briefly consider the case of spherical bubbles, where thermocapillary and solutocapillary effects play a large role.

1. Introduction

When a freezing front progresses through a liquid melt and encounters a foreign particle, the particle may be engulfed by the front, or it may be rejected and pushed ahead of the front. The outcome of this interaction plays a crucial role in issues such as the strength of composites (Mortensen & Jin 1992; Asthana 1998; Deville *et al.* 2006), the geomorphology of frozen landscapes (Dash, Rempel & Wettlaufer 2006) and the survival of cryogenically preserved cells (Bronstein, Itkin & Ishkov 1981; Ishiguro & Rubinsky 1994; Karlsson & Toner 1996; Chang *et al.* 2007). Thus, a good understanding of the particle–front interaction is essential in understanding these and other processes.

The interaction between particles and freezing fronts has received much attention over the years (e.g. Uhlmann, Chalmers & Jackson 1964; Aubourg 1978; Körber *et al.* 1985; Asthana & Tewari 1993; Asthana 1998; Park, Golovin & Davis 2006). Studies of particle capture may be classified as dealing with either engulfment by an initially planar interface, or geometrical inclusion by dendrites. Past theoretical models have generally considered the simpler planar front, as do we. Even so, there are many physical processes involved. Particle engulfment or rejection depends on liquid drag, intermolecular forces, heat flux, interfacial energies, particle geometry, interfacial premelting and, in the case of binary solidification, solute transport and constitutional undercooling.

† Present address: Massachusetts Institute of Technology, Cambridge, MA, USA. E-mail address for correspondence: kaoj@mit.edu

‡ Professor Alexander A. Golovin passed away on 10 September 2008.

Accordingly, many models have been proposed. Asthana & Tewari (1993) reviewed the field and concluded that an early model by Chernov, Temkin & Mel'nikova (1976, 1977) was relatively accurate in predicting critical speeds for experimental particle capture in pure liquids. In that formulation, van der Waals repulsion and fluid drag are balanced to obtain an instantaneous particle speed as a function of particle distance from the front. The largest attainable particle speed is then the 'critical speed' – freezing fronts moving at a faster rate will eventually overtake and engulf the particle. Subsequent work by Rempel & Worster (1999, 2001) employed more accurate drag approximations, removed assumptions on interfacial geometry and considered the effects of interfacial energy, whereas Park *et al.* (2006) considered the additional effects of density changes upon solidification and Marangoni effects (the latter in the case of bubbles rather than solid particles). The stability of the solid–liquid interface was explored by Hadji (1999, 2002, 2003), and other authors (Azouni & Casses 1998; Catalina, Mukherjee & Stefanescu 2000; Garvin & Udaykumar 2003*a*, *b*) investigated the unsteady problem, where the assumption of quasi-steady particle speed was relaxed.

Most theoretical studies, including those given above, only consider solidification of pure materials, whereas many situations of interest involve the solidification of solutions or alloys. That case has received considerably less attention in the literature despite its wide applicability. In this work, we investigate particle capture in *binary* solidification, in which solute rejection by the solid phase causes constitutional undercooling at the freezing front, thereby affecting the particle–front interaction. The primary existing theoretical treatments of particle–front interaction in binary systems are done by Temkin, Chernov & Mel'nikova (1977), Pötschke & Rogge (1989) and Sasikumar & Ramamohan (1991). Other authors have also made attempts at solving the binary system (Ahuja, Stefanescu & Dhindaw 1994; Kim & Rohatgi 1998), though these efforts are considerably rougher. Nonetheless, all previous theoretical works have involved substantial approximations to facilitate the derivation of analytical solutions. Very recently, the advent of level-set methods and fast computers has provided the opportunity for direct numerical simulation of particle capture in both pure (Garvin & Udaykumar 2005, 2006; Garvin, Yang & Udaykumar 2007*a*, *b*) and binary (Chang *et al.* 2007; Yang, Garvin & Udaykumar 2008) solidification. One can more easily measure the behaviour of particle–front systems from these simulations than from the typical experiments, and they also require fewer approximations than analytical approaches. However, they remain time consuming, are presently restricted to two-dimensional systems and do not provide any systematic exploration of particle behaviour dependence on parameters. Finally, there is a plethora of experimental results for particle inclusions in solidifying alloys, frequently in the context of metal–matrix composites (e.g. Körber *et al.* 1985; Sekhar & Trivedi 1991; Wu, Liu & Lavernia 1992; Pang, Stefanescu & Dhindaw 1994; Hecht & Rex 1997; Asthana 1998; Wilde & Perepezko 2000). Unfortunately, many of these deal with dendritic solidification or are focused on creating materials with prescribed properties rather than on investigating the fundamental mechanisms of particle capture. Moreover, due to the variety of physical phenomena that can be involved, and the challenging nature of the required experiments (Sen *et al.* 1997), it is difficult to reconcile differing experimental systems and synthesize these studies to form a broader quantitative theory of particle capture in solidification (Juretzko *et al.* 1998).

In light of this existing work, we seek to obtain systematic quantitative information about the behaviour of three-dimensional particles in solidifying binary alloys. We combine the approach of Rempel & Worster (1999, 2001), with a boundary-integral

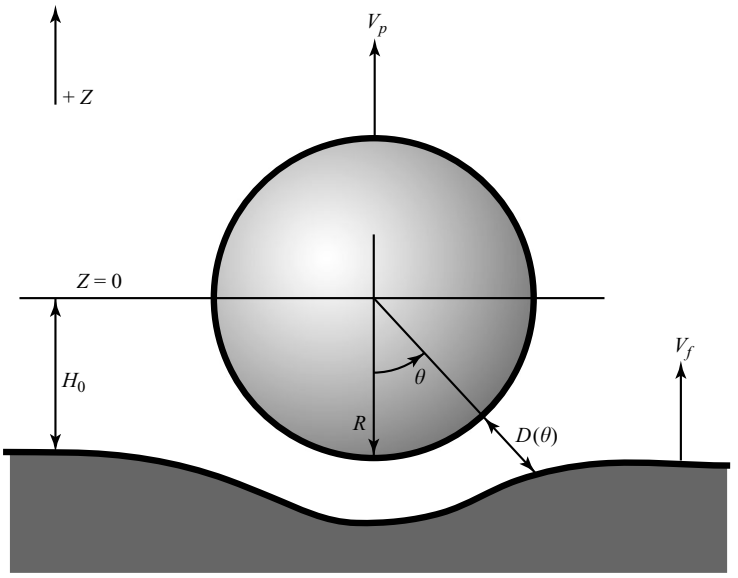

FIGURE 1. Diagram of axisymmetric particle and solidification front, showing important dimensions. H_0 is the height of the particle above the undisturbed interface, which may differ from the $T = T_m$ isotherm.

calculation of the solute concentration field and compute numerical solutions of the derived equations.

2. Governing equations

We consider a spherical particle in a three-dimensional axisymmetric particle–front system, shown in figure 1. As in Rempel & Worster (1999), the shape of the solidification front is determined by matching the interfacial temperature at thermodynamic equilibrium to a linear temperature field. The quasi-steady speed of the particle is then found through a force balance involving viscous drag, van der Waals and/or electrostatic double-layer forces and buoyancy. We allow for the possibility of differing thermal conductivities of the particle and its surroundings, as well as density changes upon solidification. For the case of freezing of bubbles, there are also thermocapillary and solutocapillary effects. Although the particular combination of equations that we present here is new, the physics of each individual piece of our model is well understood. Hence, we do not discuss the origin of these equations in detail, and instead focus on the results of their combination.

2.1. *Solute concentration*

Let ρ and θ be spherical coordinates centred on the particle (figure 1). The solute concentration $C(\rho, \theta)$ is governed by convection and diffusion, with rejection at the solidification front and no flux through the particle,

$$\partial_t C + (\boldsymbol{U} \cdot \nabla) C = D_C \nabla^2 C \quad \text{in the melt,} \tag{2.1a}$$

$$D_C \nabla C \cdot \boldsymbol{n}_f = -C(1-k)\boldsymbol{V}_f \cdot \boldsymbol{n}_f \quad \text{at the front,} \tag{2.1b}$$

$$\nabla C \cdot \boldsymbol{n}_p = 0 \quad \text{at the particle,} \tag{2.1c}$$

$$C \to C_\infty \quad \text{as } Z \to \infty, \tag{2.1d}$$

where $\boldsymbol{U}$ is the fluid velocity in the lab frame, $\boldsymbol{V}_f$ is the front velocity in the lab frame, k is the segregation coefficient, D_C is the solute diffusion coefficient, C_∞ is the concentration at infinity and $\boldsymbol{n}_f$ and $\boldsymbol{n}_p$ are the outward normals on the solidification front and particle, respectively. We are interested in quasi-steady states, so (2.1a) becomes $-V_f C_Z + (\boldsymbol{U}\cdot\nabla)C = D_C\nabla^2 C$.

Previous authors have frequently taken C to be constant in the vertical or radial direction. While this is a good approximation directly underneath the particle, the far-field condition for C is exponential decay in the vertical direction, and constant *horizontally*. Likewise, we expect that the true gradient of C near the particle (but not directly underneath it) will be neither horizontal nor vertical, but oblique. Thus, we do not make any assumptions on C at this point.

2.2. *Interfacial shape*

For slow solidification, we use the frozen-temperature approximation (Chernov *et al.* 1977), which assumes a quasi-steady temperature distribution with instantaneous diffusion of latent heat,

$$T(\rho,\theta) = T_m + G_T\left\{\left[1+\frac{k_0-k_p}{2k_0+k_p}\left(\frac{R}{\rho}\right)^2\right]Z + H\right\}. \tag{2.2}$$

Here, G_T is the imposed or far-field temperature gradient, T_m is the equilibrium melting temperature, R is the radius of the particle and k_p and k_0 are the thermal conductivities of the particle and the surrounding material, respectively. We make the approximation that the thermal conductivity of the surrounding material is k_0 in both liquid and solid phases. Z is the vertical coordinate ($Z=-\rho\cos\theta$), and the T_m isotherm is located at $Z=-H$ far from the particle.

The interfacial temperature is the equilibrium melting temperature as modified by the generalized Gibbs–Thompson effect (Ratke & Voorhees 2002), and constitutional and kinetic undercooling (Davis 2001), giving,

$$T_i = T_m\left[1-\frac{\Delta P_{s\ell}}{L_V}-\left(1-\frac{\rho_s}{\rho_\ell}\right)\frac{\Delta P_{\ell 0}}{L_V}\right] + mC - \frac{V_n}{\mu}, \tag{2.3}$$

where L_V is the latent heat per solid volume, ρ_s, ρ_ℓ are the densities, m is the liquidus slope, V_n is the speed of the front in the normal direction and μ the kinetic coefficient. $\Delta P_{s\ell}$ is the pressure difference between solid and liquid phases at the interface, and $\Delta P_{\ell 0}$ is that in the liquid phase between the interface and the far field. The solid–liquid pressure jump in this system is due to van der Waals forces (Israelachvili 1991) and surface tension, giving,

$$\Delta P_{s\ell} = \frac{A}{6\pi D^3} + \Gamma\kappa. \tag{2.4}$$

Here, A is the Hamaker constant, D is the radial distance between the particle and the interface, Γ is the interfacial energy and κ is the curvature. When ionic solutes are present, there may also be an entropic pressure at the interface, due to compression of the electrostatic double layer by the proximity of the particle. Since this is a pressure acting on counterions in a thin layer on the *liquid* side of the solidification front, we account for it in $\Delta P_{\ell 0}$, the additional liquid pressure above atmospheric at the front. For a 1:1 electrolyte (where the ions each have unit charge) in the weak overlap approximation (Israelachvili 1991),

$$\Delta P_{\ell 0} = \Omega \mathrm{e}^{-\kappa_D D}, \tag{2.5}$$

where κ_D is the inverse Debye length, and Ω is a parameter approximating the strength of the double layer. Ω is bounded by $64k_BT(N_A/M)C$ and the inverse Debye length κ_D is $\sqrt{2N_AC\mathrm{e}^2/M\epsilon_r\epsilon_0k_BT}$. We do not attempt a more precise determination of Ω, as such would require knowledge of the electric potential on the solidification front and on the particle. In addition, although both κ_D and Ω depend on the interfacial solute concentration and temperature, we calculate κ_D and Ω as constants using the approximations $T \approx T_m + mC_\infty/k$ and $C \approx C_\infty/k$ because it will be seen that the *relative* variation in these quantities is small. Finally, note that when an electrostatic double layer is present, ionic solutes form a thin layer of higher concentration at the interface, magnifying the constitutional undercooling. We neglect this effect, since it can be incorporated into the liquidus slope m.

Combining (2.2) and (2.3) with $\rho = R + D(\theta)$ yields a second-order ODE for the interface shape, given by the function $D(\theta)$. Far away from the particle, the freezing front is planar and located at $Z = -H_0$, where in general $H_0 \neq H$ due to undercooling of the front. The boundary conditions are then $D'(0) = 0$ and $H_0 - (R + D)\cos\theta \to 0$ as $\theta \to \pi/2$. Because H_0 is defined as the position of the front far from the particle, we find in terms of H,

$$H_0 = H - \frac{mC_\infty}{G_Tk} + \frac{V_f}{G_T\mu}. \tag{2.6}$$

2.3. *Particle speed*

The particle experiences forces due to viscous drag, van der Waals and double-layer repulsions and buoyancy. Buoyancy is given by $F_g = -(4/3)\pi R^3(\rho_p - \rho_\ell)g$, where ρ_p and ρ_ℓ are the densities of the particle and melt, and g is the acceleration of gravity. The other forces may be calculated as integrals of their respective pressures,

$$F = 2\pi \int_0^{\pi/2} PR^2 \sin\theta\cos\theta \,\mathrm{d}\theta. \tag{2.7}$$

Because we are primarily interested in conditions for particle capture, we assume that the particle is sufficiently close to the solidification front, such that viscous drag may be calculated using a lubrication approximation (Rempel & Worster 1999). Then, to leading order, the fluid flow between the particle and the front is tangential with speed,

$$U(\rho,\theta) = \frac{1}{2\eta\rho}(\rho - R)(\rho - R - D)\frac{\partial P_{visc}}{\partial\theta}, \tag{2.8}$$

where η is the viscosity of the fluid and P_{visc} is its pressure. Calculating flux through a surface of constant θ, we obtain $q(\theta) = 2\pi\sin\theta\int_R^{R+D} U(\rho,\theta)\rho\,\mathrm{d}\rho = -(\pi/6\eta)\sin\theta D^3\partial P_{visc}/\partial\theta$. Conservation of mass under the particle gives $q(\theta) = -\pi(R\sin\theta)^2[V_p - (1 - \rho_s/\rho_\ell)V_f]$, so solving for P_{visc} gives,

$$P_{visc} = -6\eta[V_p - (1 - \rho_s/\rho_\ell)V_f]R^2\int_\theta^{\pi/2} D^{-3}\sin\theta\,\mathrm{d}\theta. \tag{2.9}$$

As before, the van der Waals pressure is

$$P_{vdW} = \frac{A}{6\pi D^3}, \tag{2.10}$$

and the double-layer repulsion is

$$P_{DL} = \Omega\mathrm{e}^{-\kappa_D D}. \tag{2.11}$$

Requiring $F_{vdW} + F_{DL} + F_{visc} + F_g = 0$ yields an expression for the particle speed V_p as a function of the parameters, the solute concentration and the particle–front configuration.

We also allow for the possibility of the solidification front meeting a spherical bubble containing a passive gas, rather than a solid particle. In this case, the appropriate boundary condition at the bubble surface is no stress, $-\eta(\partial U/\partial\rho) = (1/R)(\partial\sigma/\partial\theta)$, and the liquid velocity becomes $U^b(\rho,\theta) = ((1/2)\eta\rho)(\rho - R - D)(\rho - R + D)\partial P^b_{visc}/\partial\theta - (1/\eta\rho)(\rho - R - D)\partial\sigma/\partial\theta$. Here σ is the liquid–gas surface tension, and the scalar U is the tangential component of liquid velocity. We obtain,

$$P^b_{visc} = -\frac{3}{2}\eta[V_p - (1-\rho_s/\rho_\ell)V_f]R^2\int_\theta^{\pi/2} D^{-3}\sin\theta\,\mathrm{d}\theta - \frac{3}{2}\int_\theta^{\pi/2}\frac{\partial\sigma}{\partial\theta}D^{-1}\,\mathrm{d}\theta, \quad (2.12)$$

and further assume that surface tension depends linearly on solute concentration and temperature, i.e.

$$\frac{\partial\sigma}{\partial\theta} = \frac{\partial\sigma}{\partial T}\frac{\partial T}{\partial\theta} + \frac{\partial\sigma}{\partial C}\frac{\partial C}{\partial\theta}, \quad (2.13)$$

where $\partial\sigma/\partial T$ and $\partial\sigma/\partial C$ are constants.

2.4. *Scaling and non-dimensionalization*

As in Rempel & Worster (1999), we non-dimensionalize distances according to $h_0 = H_0/R$, $z = Z/R$ and $\delta = D/\epsilon R$, and speeds as $v_p = V_p/W$, $v_f = V_f/W$, with $\epsilon^4 = AT_m/6\pi L_V G_T R^4$ and $W^4 = A^3 L_V G_T/6^7\pi^3\eta^4 R^4 T_m$. We express the concentration as

$$C = \frac{C_\infty}{k}c = \frac{C_\infty}{k}[c_0 + (1-k)v_f Pe\, c_1], \quad (2.14)$$

where $c_0 = 1 - (1-k)[1 - \exp(-Pe v_f(z + h_0))]$ is the one-dimensional concentration field for binary solidification in the absence of a particle and Pe is the Péclet number.

Typical values of the dimensional parameters are shown in table 1, and the corresponding non-dimensional parameters are in table 2. It is seen that for small particles in common systems, $Pe \ll 1$ and $\bar{m} \gg 1$, so we expand in powers of Pe, retaining terms of $O(\bar{m}Pe)$, to obtain

$$\nabla^2 c_1 = 0, \quad (2.15a)$$

$$h_0 - \left[1 + \epsilon\delta + \frac{\bar{k}}{1+\epsilon\delta}\right]\cos\theta = -\frac{\epsilon}{\delta^3} - \bar{m}Pe v_f\,[c_1 + (1+\epsilon\delta)\cos\theta - h_0] - \bar{\rho}\omega \mathrm{e}^{-\bar{\kappa}_D\epsilon\delta} - \gamma\bar{\kappa} + v_f\bar{\mu}^{-1}(1 - \boldsymbol{z}\cdot\boldsymbol{n}_f), \quad (2.15b)$$

$$v_p = \bar{\rho}v_f + \left[\int_0^{\pi/2}(\epsilon\delta^{-3} + \omega\mathrm{e}^{-\bar{\kappa}_D\epsilon\delta})\sin\theta\cos\theta\,\mathrm{d}\theta - \bar{g}\right] \Bigg/ \int_0^{\pi/2}\delta^{-3}\tfrac{1}{2}\sin^3\theta\,\mathrm{d}\theta, \quad (2.15c)$$

with boundary conditions $\delta'(0) = 0$, $h_0 - (1+\epsilon\delta)\cos\theta \to 0$ as $\theta \to \pi/2$, $\nabla c_1\cdot\boldsymbol{n}_f = 0$ on the front, $\nabla c_1\cdot\boldsymbol{n}_p = \boldsymbol{z}\cdot\boldsymbol{n}_p$ on the particle and $c_1 \to 0$ as $|\boldsymbol{x}| \to \infty$. The non-dimensional curvature is

$$\bar{\kappa} = \frac{-1}{1+\epsilon\delta}\left\{2 + 3\left(\frac{\epsilon\delta'}{1+\epsilon\delta}\right)^2 - \frac{\epsilon\delta''}{1+\epsilon\delta} - \left[\left(\frac{\epsilon\delta'}{1+\epsilon\delta}\right)^3 + \frac{\epsilon\delta'}{1+\epsilon\delta}\right]\cot\theta\right\} \Bigg/ \left[1 + \left(\frac{\epsilon\delta'}{1+\epsilon\delta}\right)^2\right]^{3/2}. \quad (2.16)$$

Symbol	Description	Saline (bubble)	Al–Cu (bubble)
R	Particle radius (m)	10^{-5}	10^{-5}
G_T	Temperature gradient (K m^{-1})	10^4	10^4
T_m	Melting temperature (K)	273	930
L_V	Latent heat (J m^{-3})	3.3×10^8	9.5×10^8
A	Hamaker constant (J)	1×10^{-20}	1×10^{-20}
m	Liquidus slope (K m^3 kg^{-1})	-0.09	-0.1
D_C	Solute diffusion coefficient (m^2 s^{-1})	1×10^{-9}	3×10^{-9}
C_∞	Far-field solute concentration (kg m^{-3})	9	48
k	Segregation coefficient	0.12	0.14
Γ	Interfacial energy (J m^{-2})	0.03	0.16
μ	Kinetic coefficient (m K^{-1} s^{-1})	4×10^{-6}	0.2
η	Viscosity (Pa s)	1.8×10^{-3}	1.4×10^{-3}
ρ_ℓ	Liquid density (kg m^{-3})	1×10^3	2.4×10^3
ρ_s	Solid density (kg m^{-3})	9.2×10^2	2.6×10^3
ρ_p	Particle density (kg m^{-3})	1×10^3 (1.3)	2.4×10^3 (0.38)
k_0	Liquid thermal conductivity (W m^{-1} K^{-1})	0.56	95
k_p	Particle thermal conductivity (W m^{-1} K^{-1})	0.56 (0.02)	95 (0.06)
Ω	Double-layer strength (J m^{-3})	$\leqslant 1.8\times10^8$	–
κ_D^{-1}	Debye length (m)	2.7×10^{-10}	–
$\partial\sigma/\partial T$	Thermocapillary (J m^{-2} K^{-1})	(-1.4×10^{-4})	(-1.5×10^{-4})
$\partial\sigma/\partial C$	Solutocapillary (J m kg^{-1})	(3.7×10^{-5})	(3.0×10^{-5})
W	Velocity scale (m s^{-1})	3.4×10^{-7}	4.5×10^{-7}
V_{MS}	Mullins–Sekerka speed (m s^{-1})	1.49×10^{-6}	8.80×10^{-7}

TABLE 1. Typical values of physical parameters. Most values are obtained from Kurz & Fisher (1992) and Rempel & Worster (2001). Kinetic coefficients are rough estimates based on Wettlaufer, Worster & Huppert (1997) and Hoyt & Asta (2002). k_0 is taken from the thermal conductivity in the liquid phase. Ω and κ_D in this table are calculated as described in the text. Thermocapillary and solutocapillary coefficients are estimated from Lide (1991) and Poirier & Speiser (1987). Values for a bubble are indicated in (parentheses) where they differ. The Mullins–Sekerka threshold for front stability is computed according to Mullins & Sekerka (1964), ignoring density change, kinetic undercooling and the electrostatic double layer.

For a bubble, (2.15*c*) becomes

$$v_b = \bar{\rho} v_f + 4\left[-\int_0^{\pi/2}\left(\frac{\alpha}{\epsilon}(1+\bar{k})\sin\theta + \frac{\beta}{\epsilon}v_f Pe\frac{\partial}{\partial\theta}\left[c_1^b+\cos\theta\right]\right)\frac{1}{2}\sin^2\theta\delta^{-1}\,\mathrm{d}\theta\right.$$
$$\left.+\int_0^{\pi/2}\left(\epsilon\delta^{-3}+\omega \mathrm{e}^{-\bar{\kappa}_D\epsilon\delta}\right)\sin\theta\cos\theta\,\mathrm{d}\theta - \bar{g}\right]\Bigg/\int_0^{\pi/2}\delta^{-3}\frac{1}{2}\sin^3\theta\,\mathrm{d}\theta. \qquad (2.17)$$

Note that (2.17) requires the solute concentration at the bubble, rather than at the solidification front. We denote the concentration at the bubble as c_1^b, to emphasize this fact.

3. Numerical implementation

The primary numerical challenge for this system is solving the Laplace equation (2.15*a*) on a semi-infinite and nearly singular domain that includes a narrow gap between the particle and the solidification front. We can formulate the solution to

Parameter		Definition	Saline (bubble)	Al–Cu (bubble)
ϵ	Hamaker constant	$(AT_m/6\pi L_V G_T R^4)^{\frac{1}{4}}$	1.4×10^{-3}	1.5×10^{-3}
$\bar{m}$	Liquidus slope	$-mC_\infty(1-k)/kG_T R$	59	290
Pe	Solute Péclet number	WR/D_C	3.4×10^{-3}	1.5×10^{-3}
γ	Interfacial energy	$\Gamma T_m/L_V G_T R^2$	0.025	0.16
$\bar{\mu}^{-1}$	Kinetic undercooling	$W/\mu G_T R$	0.85	2.3×10^{-5}
ω	Double-layer strength	$\Omega T_m/L_V G_T R$	$\leqslant 1.5\times10^{3}$	–
$\bar{\kappa}_D^{-1}$	Debye length	κ_D^{-1}/R	2.7×10^{-5}	–
$\bar{\rho}$	Density change	$1-\rho_s/\rho_\ell$	0.083	−0.083
$\bar{g}$	Buoyancy	$(2/3)(\rho_p-\rho_\ell)gT_m/L_V G_T$	$0\,(-5.4\times10^{-7})$	$0\,(-1.5\times10^{-6})$
$\bar{k}$	Thermal conductivity	$(k_0-k_p)/(2k_0+k_p)$	0 (0.5)	0 (0.5)
α	Thermocapillary	$\frac{3}{2}\frac{\partial\sigma}{\partial T}T_m/L_V R$	(-1.7×10^{-5})	(-2.2×10^{-5})
β	Solutocapillary	$\frac{3}{2}\frac{\partial\sigma}{\partial C}T_m C_\infty(1-k)/kL_V G_T R^2$	(3.0×10^{-3})	(1.2×10^{-2})

TABLE 2. Non-dimensional parameters for representative systems.

(2.15*a*) as a single-layer potential over the freezing front and the particle,

$$c_1(\boldsymbol{x}) = \int_{\partial\Omega} \lambda(\boldsymbol{\xi}) G_0(\boldsymbol{x};\boldsymbol{\xi})\,\mathrm{d}A_\xi, \tag{3.1}$$

where $G_0(\boldsymbol{x};\boldsymbol{\xi}) = -1/4\pi|\boldsymbol{x}-\boldsymbol{\xi}|$ is the free-space Green's function. The unknown potential density λ satisfies to $O(Pe)$ the integral equation

$$\frac{1}{2}\lambda(\boldsymbol{x}) + \int_{\partial\Omega} \lambda(\boldsymbol{\xi})\nabla_x G_0(\boldsymbol{x};\boldsymbol{\xi})\cdot\boldsymbol{n}(\boldsymbol{x})\,\mathrm{d}A_\xi = \begin{cases} 0 & \text{if } \boldsymbol{x} \text{ on the particle,} \\ z\cdot\boldsymbol{n}(\boldsymbol{x}) & \text{if } \boldsymbol{x} \text{ on the front.} \end{cases} \tag{3.2}$$

Here Ω designates the melt, $\boldsymbol{x}\in\partial\Omega$, and $\boldsymbol{n}(\boldsymbol{x})$ is the unit normal pointing into the melt. On the axis $\theta=0$, we require that the single-layer potential be smooth. The axisymmetric double integral over area $\partial\Omega$ is reduced to a single integral over θ as in Miksis (1981) and Miksis, Vanden-Broeck & Keller (1981). The boundary integral gives rise to both logarithmic and removable singularities as $\xi\to x$, as well as to highly peaked 'nearly singular' integrands due to small separations between the particle and the freezing front. We employ the method of Longuet-Higgins & Cokelet (1976) to regularize both logarithmic and near-singular terms: an integral of the form $\int H(x)f(x)\,\mathrm{d}x$, where $H(x)$ is smooth and $f(x)$ contains a logarithmic or near singularity at $x=x_0$, can be written as

$$\int H(x)f(x)\,\mathrm{d}x = \int H(x)[f(x)-g(x)]\,\mathrm{d}x + \int [H(x)-H^N(x)]g(x)\,\mathrm{d}x + \int H^N(x)g(x)\,\mathrm{d}x, \tag{3.3}$$

where $H^N(x)$ is the Taylor expansion of $H(x)$ at x_0 of the order N, and $g(x)$ is a function such that $f(x)-g(x)$ is bounded and $\int H^N(x)g(x)\,\mathrm{d}x$ can be determined analytically. Thus, the first two integrals on the right-hand side of (3.3) can be calculated numerically using the trapezoidal rule, and the last integral is found

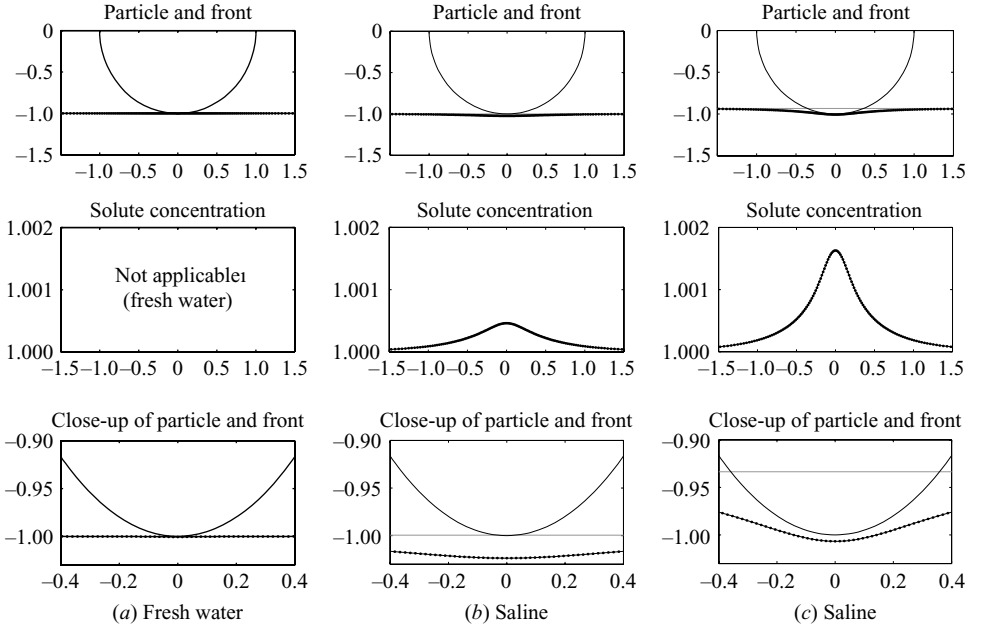

FIGURE 2. Sample particle-pushing solutions. The system is oriented the same as in figure 1. The thin grey line indicate h_0, the position of the flat front (far from the particle). The points are the calculated front location and concentration field, with the concentration field being evaluated at the front. (*a*) Particle in fresh water at $h_0 = 1.0$, $v_p = 2.34$. (*b*) Particle in saline at $h_0 = 1.0$, $v_p = 0.080$. (*c*) Particle in saline at $h_0 = 0.93$, $v_p = 0.156$.

analytically. The order N of the Taylor expansion is chosen to minimize the error in the trapezoidal integration of the second integral. We use $N = 0$ and 2. Note that (3.3) was originally developed to regularize true singularities. However, in our problem one can find $g(x)$ such that (3.3) applies to near-singularities as well – we use $g(x) = 1/p(x)$ and $g(x) = \log p(x)$, where $p(x)$ is a parabola having its minimum at the point of near singularity.

Equations (2.15*b*), (2.15*c*) and (3.2) are solved for a given h_0 by finite difference collocation, using on the order of 100 mesh points for $\theta \in [0, \pi/2)$. In order to obtain better accuracy in the boundary integrals, we upsample the smooth quantities δ, c and λ using spline interpolation, before computing the discretized integrand. It is found that upsampling by a factor of 3 is sufficient. Figure 2 shows example solutions.

Solutions are obtained for a range of h_0 by means of Euler–Newton continuation in arclength, with adaptive stepping based on convergence and turning angle (Keller 1977; Allgower & Georg 1979).

4. Results and discussion

4.1. *Speed–height curve*

Equations (2.15*a*), (2.15*b*) and (2.15*c*) or (2.17) form a system for the unknowns c_1, δ and v_p, with one free parameter h_0. In contrast to the pure solidification system, the solutions in the binary case couple to the front speed v_f due to solute rejection at the solidification front and accumulation beneath the particle. (Solutions of the pure system involve v_f only if $\bar{\rho} \neq 0$.) Depending on how we choose v_f, we may calculate one of two types of solutions to the system. If we require $v_f = v_p$, so that the

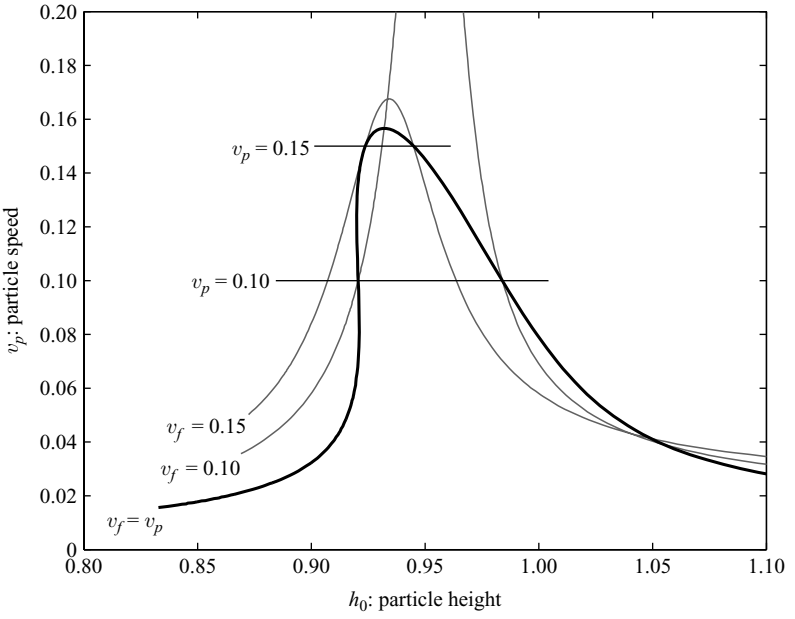

FIGURE 3. Speed versus height for a particle in saline, using parameters from table 2. We show both travelling-state and fixed-front-speed cases. The thick line indicates travelling states of the system, where $v_p = v_f$. The light lines show the particle speed v_p computed for fixed values of the front speed v_f. These curves intersect the travelling-state curve at their respective v_f's.

front and particle move together, the solutions at every h_0 correspond to quasi-steady *travelling states*, i.e. particle-pushing behaviour. However, we may also take a *fixed front speed* ($v_f = \text{constant}$), corresponding to typical experimental solidification, where the solidification rate is independent of the particle behaviour. In this case, there are at most two values of h_0 satisfying $v_f = v_p(h_0, \ldots)$, and hence most of the solutions do not correspond to travelling states, but rather to quasi-steady non-equilibrium behaviour of the particle.

Figure 3 shows particle speed versus height for the example saline system in table 2, under both travelling-state and fixed-front-speed conditions. The travelling-state curve represents all possible equilibria for the given particle and material parameters, whereas the fixed-front-speed curve provides information about the height evolution of a particle encountering a front moving at some v_f. In both cases, it is seen that if the particle and the front are far apart (h_0 is large), the particle has low speed. At closer range ($h_0 \approx 1$), the particle speed is large due to intermolecular repulsion. Finally, if $h_0 < 1$ and the particle is deep in the solid phase, the speed is again small due to viscous drag.

4.2. *Critical speed for capture*

By definition, the maximum of the travelling-state curve is the maximum of the range of possible front speeds for particle pushing. This is generally denoted as the capture or critical speed, $v_c = \max_{h_0} v_p$. No travelling states exist when $v_f > v_c$, so if a solidification front encounters a particle, the particle is overtaken and captured by the solid phase. However, at lower front speeds when $v_f < v_c$, in general a particle will be rejected from the solid phase and pushed ahead of the front. Thus, the speed

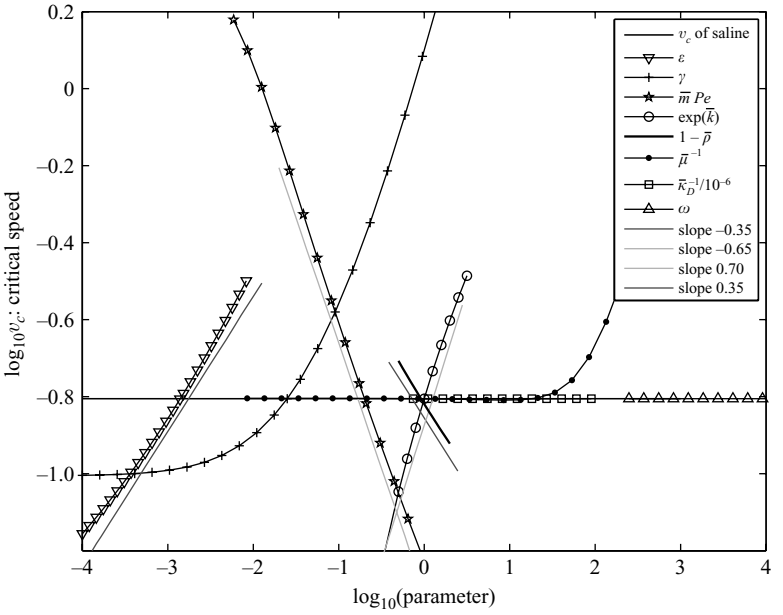

FIGURE 4. Dependence of v_c on non-dimensional parameters as varied around the nominal values for saline (table 2). The critical speed at the nominal values is shown as a thick horizontal line.

v_c and its dependence on parameters are of great interest in studies involving particle capture.

Figure 4 shows the dependence of v_c on the non-dimensional parameters, as they vary from the nominal values for saline. For a particle, $\bar{m}$ and Pe only appear jointly in the equations, so they have been combined here for convenience.† With the exceptions of γ and large values of $\bar{\mu}^{-1}$, the plotted curves for all parameters are nearly linear over large ranges of the parameter values. Based on these computations, we may determine the scaling of v_c in the vicinity of the saline parameters, with the scaling exponents found to the nearest 0.05,

$$v_c \propto \epsilon^{0.35}\gamma^{0.30}(\bar{m}\,Pe)^{-0.65}\mathrm{e}^{0.70\bar{k}}(1-\bar{\rho})^{-0.35}, \tag{4.1}$$

or equivalently in dimensional form,

$$V_c \propto R^{-1.30}G_T^{0.35}\Gamma^{0.30}\left(\frac{T_m}{L_V}\right)^{0.30}A^{0.35}\eta^{-0.35}\left(\frac{\rho_s}{\rho_\ell}\right)^{-0.35} \times\left(\frac{|m|C_\infty(1-k)}{D_c k}\right)^{-0.65}\exp\left(0.70\frac{k_0-k_p}{2k_0+k_p}\right). \tag{4.2}$$

We find little or no dependence on the parameters $\bar{\mu}^{-1}$, $\bar{\kappa}_D^{-1}$, and ω, representing kinetic undercooling and the electrostatic double layer. However, the dependence on γ, representing interfacial energy, is more complex than is made apparent by (4.1). The $\gamma^{0.30}$ scaling in (4.1) is the local slope near our model saline system, $\gamma = 0.025$, and does not hold for significantly different values of γ. For instance, if we ignore

† The combination $M = \bar{m}Pe\,v_f$ is sometimes referred to as the morphological number in studies of interfacial stability. However, we are only concerned with planar solidification in this work.

surface tension or assume its effect is negligible, $v_c \propto \gamma^0$, and (4.2) becomes

$$V_c \propto R^{-0.70} G_T^{0.65} \ldots, \tag{4.3}$$

with no dependence on melting temperature T_m, latent heat L_V or interfacial energy Γ. Whereas, if we take $v_c \propto \gamma^{0.75}$ corresponding to large γ, we obtain,

$$V_c \propto R^{-2.20} G_T^{-0.10} \left(\frac{\Gamma T_m}{L_V} \right)^{0.75} \ldots. \tag{4.4}$$

In general, for $v_c \propto \gamma^{a(\gamma)}$ where the exponent a is a slowly changing function of γ,

$$V_c \propto R^{-0.70-2a} G_T^{0.65-a} \left(\frac{\Gamma T_m}{L_V} \right)^{a} \ldots. \tag{4.5}$$

In (4.3)–(4.5), terms that remain unchanged from (4.2) have been omitted. Further, in all cases the kinetic undercooling and electrostatic double layer are found to be too weak to affect the capture speed. We attribute the lack of influence of the kinetic undercooling to the fact that it acts over the entire interface, not merely the portion under the particle, while the double layer has little effect because the Debye length is smaller than van der Waals premelting distances for our parameters. Finally, note that figure 4 shows the results of varying one non-dimensional parameter at a time, while keeping all others constant. Therefore, (4.1) and subsequent variations do not encapsulate effects that arise from changing multiple parameters simultaneously; for example, if the thermal conductivity of the particle was less than that of the melt ($\bar{k} > 0$), the solidification front may become convex, and increasing the interfacial energy then lowers the critical speed rather than raising it.

The predictions of (4.3) and (4.4) may be compared to previous work on binary particle capture. The following equations are rewritten in our notation for convenience. Temkin *et al.* (1977) obtained an expression,

$$V_c \approx 1.3 R^{-2} \left(\frac{\Gamma T_m}{L_V} \right) \left(\frac{|m| C_\infty}{k D_C} \right)^{-1} \Bigg/ \log \left(18\pi\eta \frac{k D_C}{|m| C_\infty} \frac{\Gamma T_m}{A L_V} \right), \tag{4.6}$$

making the assumption that the effect of G_T is negligible. Later, Pötschke & Rogge (1989) ignored the Gibbs–Thomson undercooling due to interfacial energy, and fitted a function to their numerical results in an intermediate range of parameters

$$V_c \approx 0.053 R^{-1} \sqrt{\frac{A G_T D_C k}{\eta |m| C_\infty} \frac{k_p}{k_0}}. \tag{4.7}$$

(Sasikumar & Ramamohan 1991, do not present any scaling results, but show a graph which appears to give $V_c \propto C_\infty^{-1}$.) Clearly (4.6) and (4.7) differ substantially; this was noted by Pötschke & Rogge (1989), but not fully explained. However, by comparing these scalings to our numerical results (4.3) and (4.4), we find that much of the difference between Temkin *et al.* (1977) and Pötschke & Rogge (1989) may be attributed to the presence or absence of interfacial energy, i.e. the dependence on γ. It is also worth pointing out that for typical parameter values of saline (table 2), we compute an entirely different scaling than either previous work, namely (4.2), and this behaviour persists for roughly a factor of 10 in either direction in the value of γ (figure 4). Hence, we expect that a large range of experimental setups may display behaviour not described by either of the previous works, but rather by some form of

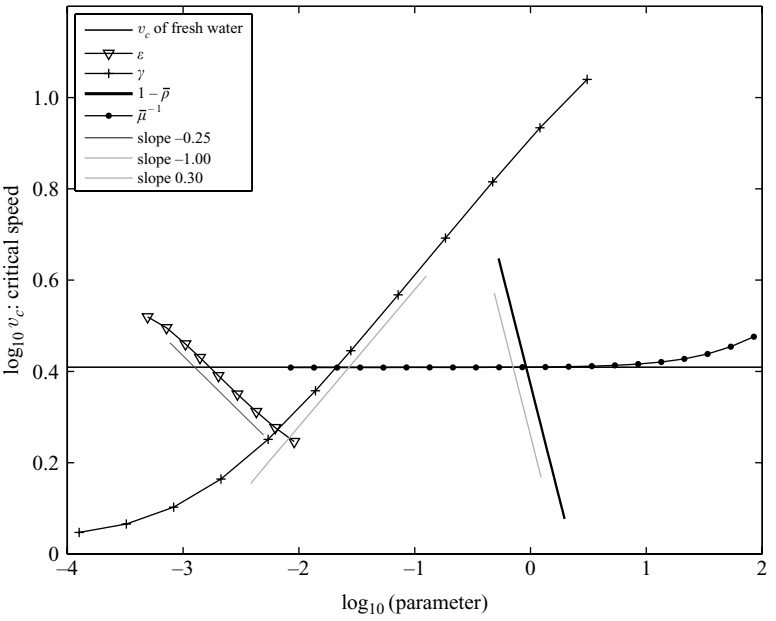

FIGURE 5. Dependence of v_c on non-dimensional parameters as varied around nominal values for fresh water. The critical speed at the nominal values is shown as a horizontal line. The apparent negative correlation with van der Waals strength (ϵ) is a consequence of the speed scaling – the dimensional dependence on van der Waals repulsion is found to be $V_c \propto A^{0.69}$.

(4.5), e.g. (4.2). In general, the relationship between V_c and R may change significantly depending on the influence of interfacial energy on the front shape.

On the other hand, all predicted capture speeds are quite similar. Using parameters for the saline system (table 1), our calculations yield $V_c = 5.3 \times 10^{-8}\,\mathrm{m\,s^{-1}}$. Evaluating (4.6) gives $V_c = 1.7 \times 10^{-7}\,\mathrm{m\,s^{-1}}$ and (4.7) gives $V_c = 1.5 \times 10^{-8}\,\mathrm{m\,s^{-1}}$. However, we consider the precise numerical values to be less important than the scaling behaviour, because several of the parameters required for the calculation are known only approximately.

For our nominal parameters for aluminium–copper, we obtain, $v_c \propto \epsilon^{0.25}\gamma^{0.50}(\bar{m}Pe)^{-0.75}\mathrm{e}^{0.50\bar{k}}(1-\bar{\rho})^{-0.25}$, where again the exponent on γ is taken locally and kinetic undercooling and electrostatic double-layer effects are negligible. This translates to a dimensional scaling of

$$V_c \propto R^{-1.50} G_T^{0.25} \left(\frac{\Gamma T_m}{L_V}\right)^{0.50} A^{0.25}\eta^{-0.25}\left(\frac{\rho_s}{\rho_\ell}\right)^{-0.25} \times \left(\frac{|m|C_\infty(1-k)}{D_c k}\right)^{-0.75} \exp\left(0.50\frac{k_0-k_p}{2k_0+k_p}\right), \quad (4.8)$$

which is reasonably similar to the saline scaling (4.2).

We also compute the v_c scaling of fresh water, for verification and comparison. This is shown in figure 5. We obtain $v_c \propto \epsilon^{-0.25}\gamma^{0.30}(1-\bar{\rho})^{-1}$ and in dimensional form

$$V_c \propto R^{-1.35} G_T^{0.01}\Gamma^{0.30} A^{0.69}\eta^{-1}\left(\frac{\rho_s}{\rho_\ell}\right)^{-1}. \quad (4.9)$$

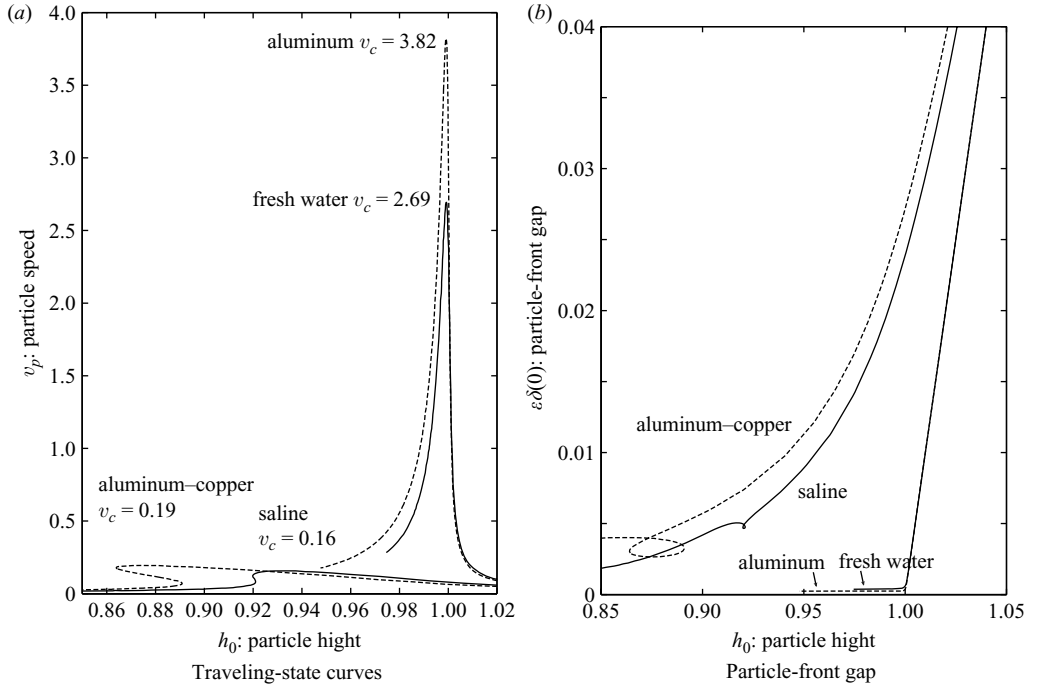

FIGURE 6. Comparison of pure and binary systems. (*a*) The presence of solute reduces particle speeds dramatically. (*b*) Particle–front gap as a function of particle height for pure and binary systems (under the travelling-state condition). The gap is greatly increased for binary systems. The loops are due to the multi-valued nature of the speed–height curves as seen in (*a*).

These results compare well with the findings of Rempel & Worster (2001), who found $V_c \propto R^{-4/3}\Gamma^{1/3}A^{2/3}\eta^{-1}$ and no dependence on G_T. The good agreement here in the pure case suggests that a closer examination of the differences between our findings and previous work in the binary case may be worthwhile.

4.3. *Effects of solute*

Perhaps the most important effect of solute in a particle–front system is a drastic reduction in particle speeds. Due to the large value of the non-dimensional liquidus slope, the effect of solute accumulation beneath the particle is strong, even though the relative change in solute concentration may be less than 1 %. The net result is to significantly impede the solidification front below the particle. Thus, although van der Waals repulsion provides the force pushing the particle, the strength of this force is governed by the particle–front gap, which in turn is strongly determined by solute concentration and the resulting undercooling. Solute, therefore, increases the gap and reduces considerably the effect of the repulsive van der Waals force. Figure 6(*a*) shows that this results in particle speeds an order of magnitude slower in the binary system than in the pure system.

By consideration of the parameters in the non-dimensionalized equation (2.15*b*), it is seen that a calculation of particle capture in any system that may contain impurities must take into account the solute effect (i.e. constitutional undercooling) whenever $\epsilon \lesssim \bar{m}Pe$, or equivalently, if $(AT_m/6\pi L_V G_T R^4)^{1/4} \lesssim |m|C_\infty(1-k)/kG_T R$. This is the case in our example system, where $\epsilon = 0.0014$ and $\bar{m}Pe = 0.20$. Figure 6(*b*) shows the particle–front gap as a function of particle height for both fresh water and saline

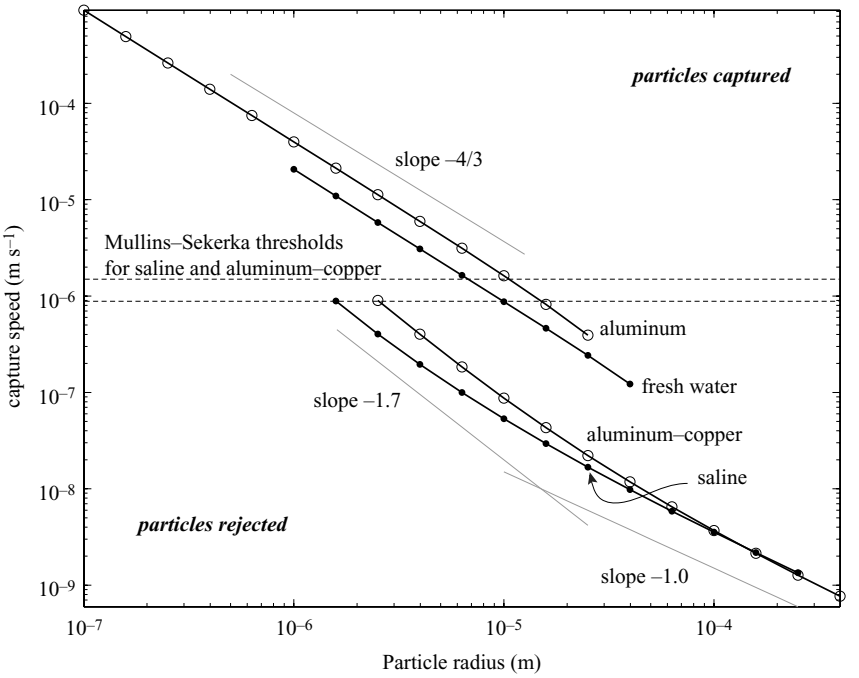

FIGURE 7. The capture or rejection of particles as a function of particle radius and solidification front speed. Systems above and to the right of the lines display particle capturing behaviour, while systems below and to the left display particle-pushing behaviour. There is a significantly sized region where particles may be pushed in a pure system but captured in a binary system. The Mullins–Sekerka stability thresholds are shown as dashed lines.

cases. The strong effect of constitutional undercooling is apparent. (The loops in the curves for binary systems are due to the multi-valued nature of the speed–height curves as seen in figure 6*a*.)

For a given (fixed) front speed, the critical speed V_c decreases as the particle radius R increases. Therefore, in lieu of a critical speed, for a fixed V_f we may define a critical *radius* R_c, where particles smaller than R_c are rejected and particles larger than R_c are captured, causing a segregation or sorting of particles. This is of importance, for instance, in solidification of composite materials with particles of non-uniform sizes. In figure 7, we plot the predicted fate of particles: radius versus front speed. Particles that fall to the upper right on this diagram will be captured, while particles in the lower left are rejected. Again, the difference between pure and binary systems is apparent as a large decrease in the critical speed or equivalently a decrease in the critical radius – particles falling in the middle of the diagram, between the sets of lines, are captured in a binary system but rejected by the pure system. We also see the scaling of V_c vs R in the slope of the dividing lines between capture and non-capture. In figure 7 all non-dimensional parameters are varied simultaneously as R varies, whereas in figures 4 and 5, each non-dimensional parameter is varied individually. Still, we find similar scalings as before, with the pure system obeying $V_c \propto R^{-4/3}$, and the binary system changing in behaviour between $V_c \propto R^{-1.7}$ and $V_c \propto R^{-1}$, depending on the value of R. Although a direct comparison to figure 7 is difficult due to the complexity of these systems, we refer the reader to the experimental studies Körber

et al. (1985), Ahuja *et al.* (1994) and Hecht & Rex (1997), which also present V_c vs R in binary solidification.

4.4. *Interfacial stability*

It is well known that initially planar solidification fronts in binary alloys can undergo instability, leading to a variety of morphologies, including cellular and dendritic solidification (Davis 2001). However, an investigation of the effect of a foreign particle on the stability of the front is beyond the scope of this work; many papers have been devoted to this subtopic alone (Hadji 1999, 2002, 2003). Instead, we note that the Mullins–Sekerka limits for planar stability are $V_{MS} = 1.49 \times 10^{-6}$ and $8.80 \times 10^{-7}\,\mathrm{m\,s^{-1}}$ for our representative saline and aluminium–copper systems (table 1), whereas the corresponding critical speeds for capture of an $R = 10^{-5}\,\mathrm{m}$ particle are $V_c = 5.3 \times 10^{-8}$ and $8.7 \times 10^{-8}\,\mathrm{m\,s^{-1}}$. A comparison with V_c is also shown in figure 7, for a range of particle radii. In general, the Mullins–Sekerka threshold of stability remains significantly faster than the capture speed for particles of $R = 10^{-5}\,\mathrm{m}$ and larger.

4.5. *Quasi-steady particle dynamics*

To determine the actual evolution of the particle height, one must refer to the fixed-front-speed curve, in conjunction with the relation

$$\frac{\mathrm{d}h_0}{\mathrm{d}t} = v_p - v_f. \tag{4.10}$$

For instance, at large h_0, the particle speed is small, so h_0 decreases, i.e. the front approaches the particle. As h_0 decreases, v_p increases. If $v_f < v_c$, eventually a particle height is reached such that $v_p = v_f$ and $\mathrm{d}h_0/\mathrm{d}t = 0$, i.e. the particle has settled at an equilibrium height above the front. This is a stable equilibrium, because $(\partial v_p/\partial h_0)_{v_f} < 0$. The particle is pushed ahead of the front in this position, unless an external perturbation decreases the particle height below the second (unstable) equilibrium. On the other hand, if $v_f > v_c$, $\mathrm{d}h_0/\mathrm{d}t$ is always negative, and the particle is captured even in the absence of perturbations.

In the case of particle capture, a quantity of interest is the displacement of captured particles caused by the passage of the freezing front. This plays a role in the uniformity or lack thereof of solidified composites (Hecht & Rex 1997; Asthana 1998; Dash *et al.* 2006). This displacement is calculated as $\Delta Z = \int_{-\infty}^{\infty} V_p(H_0(t))\,\mathrm{d}t$. Employing (4.10) to make a change of variables, we obtain

$$\Delta Z = \int_{-\infty}^{\infty} \frac{V_p(H_0)}{V_f - V_p(H_0)}\,\mathrm{d}H_0. \tag{4.11}$$

Clearly, it is necessary that $V_p(H_0) \to 0$ as $H_0 \to \infty$, in order for ΔZ to be bounded for a particle starting at infinity. Thus, without any finite initial position given, ΔZ can only be calculated with zero buoyancy and no solidification density change. Because both of our example systems have density change on solidification, we correct this by making the replacements $V_p \to V_p - \bar{\rho} V_f$ and $V_f \to V_f - \bar{\rho} V_f$, resulting in displacement relative to the liquid phase, rather than displacement relative to the solid phase. Finally, because the calculation of ΔZ requires the knowledge of V_p at all values of H_0, including those for which the particle is far from the front (where the lubrication approximation of drag is no longer valid), we calculate viscous drag on the particle at large H_0 by employing the result of Brenner (1961) for spheres moving perpendicularly to a wall. Because both expressions for viscous drag are expected to underestimate the drag force when used beyond their ranges of validity, V_p is taken to be the smaller of the two values calculated via lubrication and Brenner's result.

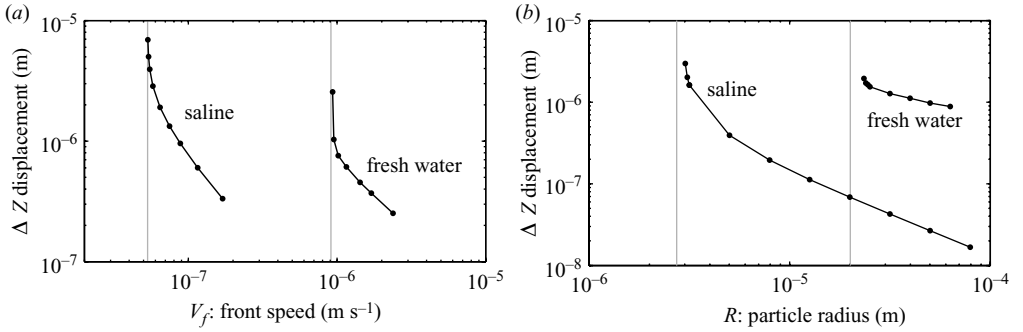

FIGURE 8. Displacement of captured particles in saline. (*a*) Displacement versus front speed at $R = 10^{-5}$ m. (*b*) Displacement versus particle radius at $V_f = 3 \times 10^{-7}\,\mathrm{m\,s^{-1}}$.

We further require that $V_p = 0$ when the particle is embedded in the solid, which is taken to correspond to $h_0 = 0$, and we approximate the van der Waals repulsion for a sphere far from the interface to be $F_{vdW} = A/6Rh_0(h_0 - 1)^2$.

Figure 8 shows the resulting displacement of captured particles as a function of radius and front speed. It can be seen that as $V_f \to V_c$, the displacement blows up, reflecting a transition to particle-pushing behaviour. The blow-up occurs as $(V_f - V_c)^{-1/2}$, assuming V_p is quadratic near its maximum. However, observe that displacements are generally smaller than the particle radius, often by orders of magnitude. This suggests that any particle experimentally observed to be moved large distances by the passage of a fixed-velocity front may have been travelling in the stable pushing state, and been captured due to an external disturbance or an effect not described by the present theory.

4.6. *Bubbles*

Finally, we have also derived equations for the case of bubbles instead of solid particles. However, the thermocapillary migration rate of bubbles is generally orders of magnitude faster than typical freezing front speeds. For example, for the saline parameters of table 1, the Young–Goldstein–Block thermocapillary speed (Young, Goldstein & Block 1959) of an $R = 10^{-5}$ m bubble is between 2.5×10^{-3} and $2.7 \times 10^{-3}\,\mathrm{m\,s^{-1}}$, depending on the orientation of the thermal field with respect to the gravity. Even the presence of a nearby solid wall only decreases the migration speed by a factor proportional to D/R at best (Meyyappan, Wilcox & Subramanian 1981). Furthermore, the presence of salt in the water exacerbates the problem because $\partial\sigma/\partial C$ is positive for this system (as well as in our other system, aluminum–copper). As the concentration gradient is negative, solutocapillary flow enhances the thermocapillary migration rather than counteracting it.

This suggests that travelling states are extremely unlikely, and so we calculate only fixed-front-speed curves for bubbles. These are shown in figure 9, for $V_f = 0.2 \times W = 6.8 \times 10^{-8}\,\mathrm{m\,s^{-1}}$, with and without solutocapillary flow, with reversed solutocapillary flow, and for a bubble in fresh water. The vertical scale is logarithmic, in order to accommodate the large range. (Some example front shapes are shown in figure 10.) Because our equations were derived for slow flows and small particle–front separations, they become increasingly inaccurate for large h_0 and large v_p. Nonetheless, we still predict large h_0 thermocapillary-only speeds of the same order of magnitude as found using the equation of Young *et al.* (1959).

For bubbles with combined thermocapillary and solutocapillary effects, and bubbles with only thermocapillary effect, it is seen that even when the bubble is deep into the

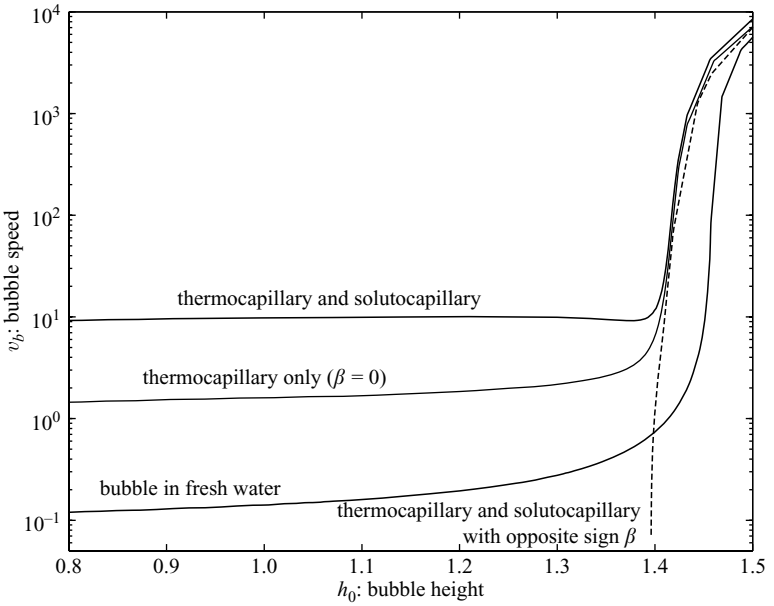

FIGURE 9. Bubble speed in saline versus height at fixed front speed $v_f = 0.2$. For saline, we show bubbles with combined thermocapillary and solutocapillary flows, bubbles with only thermocapillary flow, and bubbles with reversed solutocapillary flow. Bubbles in fresh water (which experience only thermocapillary flow) are shown for comparison. Note the logarithmic speed scale – bubble speeds are orders of magnitude faster than the front speeds, and bubbles in saline move faster than bubbles in fresh water. At smaller h_0, the solutocapillary effect contributes significantly to the flow, either imposing an effective lower bound on the bubble speed or promoting bubble capture, depending on the sign of β.

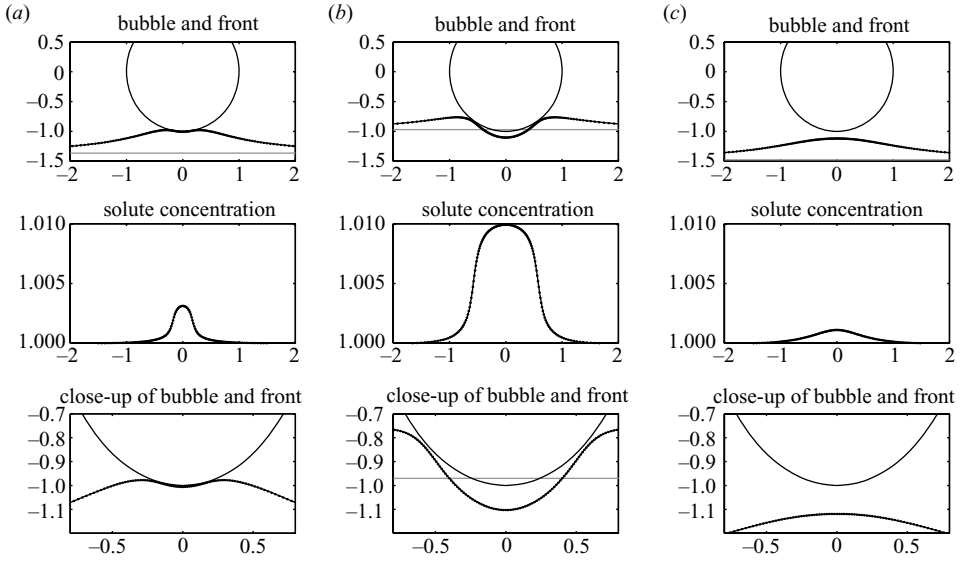

FIGURE 10. Sample front shapes and solute concentrations with nominal saline parameters. The distorted thermal field causes the front to bulge towards the bubble, while the solute accumulation pushes back the front directly beneath the bubble. (*a*) $v_f = 0.2$, $v_p = 9.27$, $h_0 = 1.36$; (*b*) $v_f = 0.4$, $v_p = 140$, $h_0 = 0.97$; (*c*) $v_f = 0.4$, $v_p = 1.3 \times 10^4$, $h_0 = 1.48$.

solid, the speed remains large, at least an order of magnitude faster than both the critical speed for particle capture and the Mullins–Sekerka stability limit of the planar interface (table 1). This high bubble speed is because capillary migration is faster if the bubble is further from the front, and constitutional undercooling due to solute accumulation ensures a large bubble–front gap. (Although not shown in figure 9, we observe that increasing the front speed enhances this effect by increasing the solute concentration at the front.) Furthermore, when significant solute accumulation exists, the solutocapillary flow greatly increases bubble speeds beyond the thermocapillary-only speeds.

On the other hand, we find that if the sign of the solutocapillary coefficient β is negative (e.g. for air bubbles in an ethanol and water mixture), the capillary migration of the bubble may reverse at small separations due to the high solute gradient, leading to capture of the bubble. This is shown as the dashed line in figure 9.

However, in all cases capillary migration increases with distance from the front; even when the travelling state exists, it is unstable. These results suggest that bubbles will be only captured in the solid if they originate extremely close to the interface, for example by nucleation. Although nucleation at the front is a common occurrence, due to lower gas solubility in the solid phase than in the liquid phase, the nucleation process is outside the scope of this work and we shall not examine this aspect in further detail. We instead refer the reader to Rogerson & Cardoso (2000) and Wei, Huang & Lee (2003) for investigations of bubble nucleation, Park *et al.* (2006) and Hadji (2007) for investigations of bubble speed in pure solidification and Wang, Mukai & Lee (1999) which examines solutocapillary migration near a solidification front (but neglects the thermal gradient).

5. Conclusion

We have examined the interaction of a foreign particle with a solidification front in a binary alloy. We have derived equations governing the system, and we have calculated the concentration field and the interface shape numerically.

We have determined the dependence on parameters of the critical speed for particle capture, and reconciled the differences between two previous results (Temkin *et al.* 1977; Pötschke & Rogge 1989) for this system. We have further found that many typical systems may obey a scaling significantly different than that indicated by the previous results, which assume either strong or negligible dependence on the interfacial energy. On the other hand, our calculations suggest that the effects of kinetic undercooling and the electrostatic double layer are insignificant in typical systems.

We have shown that the presence of solute in a particle–front system reduces particle speeds by an order of magnitude, because constitutional undercooling greatly increases the gap between the particle and the solidification front. We have compared radii and front speeds required for particle capture and rejection, for saline, fresh water, aluminium–copper alloy and pure aluminum, and found that the presence of solute makes particle capture significantly easier. We have also calculated the displacement of captured particles as a function of radius and front speed, for saline and fresh water, and found that the displacement is frequently less than the particle radius.

Finally, we have considered the case of bubbles interacting with a solidification front. In this case we found that the large capillary migration dominates the

interaction, suggesting that bubbles should be nucleated on the interface in order to be captured.

Although quantitative experimental studies of particle–front interactions remain scarce, we hope that this systematic theoretical investigation will help to fill the large gap between existing experiments and idealized analytical results.

Justin C. T. Kao was partially supported by a James R. Everly fellowship at Northwestern University. We are grateful to Professors M. J. Miksis and M. G. Worster for their advice and suggestions.

REFERENCES

Ahuja, S., Stefanescu, D. M. & Dhindaw, B. K. 1994 Role of processing/system parameters on the interactions between liquid/solid interfaces and insoluble particles. In *Proceedings of the Second International Conference on Cast Metal Matrix Composites* (ed. D. M. Stefanescu & S. Sen), pp. 44–56. American Foundrymen's Society.

Allgower, E. L. & Georg, K. 1979 *Introduction to Numerical Continuation Methods*, *Classics in Applied Mathematics*, vol. 45. Society for Industrial and Applied Mathematics.

Asthana, R. 1998 *Solidification Processing of Reinforced Metals*, *Key Engineering Materials*, vol. 151–152. Trans Tech Publications.

Asthana, R. & Tewari, S. N. 1993 The engulfment of foreign particles by a freezing interface. *J. Mater. Sci.* **28**, 5414–5425.

Aubourg, P. 1978 Interaction of second-phase particles with a crystal growing from the melt. PhD thesis, Massachusetts Institute of Technology, Cambridge, MA.

Azouni, M. A. & Casses, P. 1998 Thermophysical properties effects on segregation during solidification. *Adv. Colloid Interface Sci.* **75**, 83–106.

Brenner, H. 1961 The slow motion of a sphere through a viscous fluid towards a plane surface. *Chem. Engng Sci.* **16**, 242–251.

Bronstein, V. L., Itkin, Y. A. & Ishkov, G. S. 1981 Rejection and capture of cells by ice crystals on freezing aqueous solutions. *J. Crystal Growth* **52**, 345–349.

Catalina, A. V., Mukherjee, S. & Stefanescu, D. M. 2000 A dynamic model for the interaction between a solid particle and an advancing solid/liquid interface. *Metall. Mater. Trans.* A **31A**, 2559–2568.

Chang, A., Dantzig, J. A., Darr, B. T. & Hubel, A. 2007 Modeling the interaction of biological cells with a solidifying interface. *J. Comput. Phys.* **226** (2), 1808–1829.

Chernov, A. A., Temkin, D. E. & Mel'nikova, A. M. 1976 Theory of the capture of solid inclusions during the growth of crystals from the melt. *Soviet Phys.: Crystallogr.* **21**, 369–373.

Chernov, A. A., Temkin, D. E. & Mel'nikova, A. M. 1977 The influence of the thermal conductivity of a macroparticle on its capture by a crystal growing from a melt. *Soviet Phys.: Crystallogr.* **22**, 656–658.

Dash, J. G., Rempel, A. W. & Wettlaufer, J. S. 2006 The physics of premelted ice and its geophysical consequences. *Rev. Mod. Phys.* **78** (3), 695–741.

Davis, S. H. 2001 *Theory of Solidification*. Cambridge University Press.

Deville, S., Saiz, E., Nalla, R. K. & Tomsia, A. P. 2006 Freezing as a path to build complex composites. *Science* **311**(5760), 515–518.

Garvin, J. W. & Udaykumar, H. S. 2003*a* Particle-solidification front dynamics using a fully coupled appraoch. Part I: Methodology. *J. Crystal Growth* **252**, 451–466.

Garvin, J. W. & Udaykumar, H. S. 2003*b* Particle-solidification front dynamics using a fully coupled appraoch. Part II: Comparison of drag expressions. *J. Crystal Growth* **252**, 467–479.

Garvin, J. W. & Udaykumar, H. S. 2005 Drag on a ceramic particle being pushed by a metallic solidification front. *J. Crystal Growth* **276**, 275–280.

Garvin, J. W. & Udaykumar, H. S. 2006 Effect of a premelted film on the dynamics of particle-solidification front interactions. *J. Crystal Growth* **290**, 602–614.

Garvin, J. W., Yang, Y. & Udaykumar, H. S. 2007*a* Multiscale modeling of particle-solidification front dynamics, Part I: Methodology. *Int J. Heat Mass Transfer* **50**, 2952–2968.

Garvin, J. W., Yang, Y. & Udaykumar, H. S. 2007*b* Multiscale modeling of particle-solidification front dynamics. Part II: Pushing-engulfment transition. *Int J. Heat Mass Transfer* **50** (15–16), 2969–2980.

Hadji, L. 1999 Asymptotic analysis of particle engulfment. *Phys. Rev.* E **60** (5), 6180–6183.

Hadji, L. 2002 Modelling and asymptotic analysis of particle-interface interaction. *Math. Comput. Model.* **36**, 147–156.

Hadji, L. 2003 Morphological instability prior to particle engulfment by a solidifying interface. *Script Materialia* **48**, 665–669.

Hadji, L. 2007 Migration of a bubble in front of a directionally solidified interface. *Phys. Rev.* E **75** (4), 2602.

Hecht, U. & Rex, S. 1997 On the transition from pushing to engulfment during directional solidification of the particle-reinforced aluminum-based metal-matrix composite 2014+ 10 vol pct Al2O3. *Metall. Mater. Trans.* A **28** (3), 867–874.

Hoyt, J. J. & Asta, M. 2002 Atomistic computation of liquid diffusivity, solid–liquid interfacial free energy, and kinetic coefficient in Au and Ag. *Phys. Rev.* B **65**, 214106.

Ishiguro, H. & Rubinsky, B. 1994 Mechanical interactions between ice crystals and red blood cells during directional solidification. *Cryobiology* **31** (5), 483–500.

Israelachvili, J. N. 1991 *Intermolecular and Surface Forces*. Academic Press.

Juretzko, F. R., Stefanescu, D. M., Dhindaw, B. K., Sen, S. & Curreri, P. A. 1998 Particle engulfment and pushing by solidifying interfaces: Part I. Ground experiments. *Metall. Mater. Trans.* A **29** (6), 1691–1696.

Karlsson, J. O. M. & Toner, M. 1996 Long-term storage of tissues by cryopreservation: critical issues. *Biomaterials* **17** (3), 243–256.

Keller, H. B. 1977 Numerical solution of bifurcation and nonlinear eigenvalue problems. In *Applications of Bifurcation Theory* (ed. P. H. Rabinowitz). Academic Press.

Kim, J. K. & Rohatgi, P. K. 1998 The effect of the diffusion of solute between the particle and the interface on the particle pushing phenomena. *Acta Metallurgica* **46** (4), 1115–1123.

Körber, C., Rau, G., Cosman, M. D. & Cravalho, E. G. 1985 Interaction of particles and a moving ice-liquid interface. *J. Crystal Growth* **72** (3), 649–662.

Kurz, W. & Fisher, D. J. 1992 *Fundamentals of Solidification*. Trans Tech Publications.

Lide, D. R. (ed.) 1991 *Handbook of Chemistry and Physics*. CRC Press.

Longuet-Higgins, M. S. & Cokelet, E. D. 1976 The deformation of steep surface waves on water. I. A numerical method of computation. *Proc. Roy. Soc. Lond.* A **350**, 1–26.

Meyyappan, M., Wilcox, W. R. & Subramanian, R. S. 1981 Thermocapillary migration of a bubble normal to a plane surface. *J. Colloid Interface Sci.* **83** (1), 199–208.

Miksis, M. J. 1981 Numerical solution of hydrodynamic free boundary problems. PhD thesis, Courant Institute, New York University.

Miksis, M. J., Vanden-Broeck, J.-M. & Keller, J. B. 1981 Axisymmetric bubble or drop in a uniform flow. *J. Fluid Mech.* **108**, 89–100.

Mortensen, A. & Jin, I. 1992 Solidification processing of metal matrix composites. *Intl Mater. Rev. (USA)* **37** (3), 101–128.

Mullins, W. W. & Sekerka, R. F. 1964 Stability of a planar interface during solidification of a dilute binary alloy. *J. Appl. Phys.* **35**, 444–451.

Pang, H., Stefanescu, D. M. & Dhindaw, B. K. 1994 Influence of interface morphology on the pushing/engulfment transition of polystyrene particles in succinonitrile + water matrices. In *Proceedings of the Second International Conferences on Cast Metal Matrix Composites* (ed. D. M. Stefanescu & S. Sen), pp. 57–69. American Foundrymen's Society.

Park, M. S., Golovin, A. A. & Davis, S. H. 2006 The encapsulation of particles and bubbles by an advancing solidification front. *J. Fluid Mech.* **560**, 415–436.

Poirier, D. R. & Speiser, R. 1987 Surface tension of aluminum rich Al–Cu liquid alloys. *Metall. Mater. Trans.* A **18A**, 1156–1160.

Pötschke, J. & Rogge, V. 1989 On the behaviour of foreign particles at an advancing solid–liquid interface. *J. Crystal Growth* **94**, 726–738.

Ratke, L. & Voorhees, P. W. 2002 *Growth and Coarsening: Ostwald Ripening in Materials Processing*. Springer-Verlag.

Rempel, A. W. & Worster, M. G. 1999 The interaction between a particle and an advancing solidification front. *J. Crystal Growth* **205**, 427–440.

Rempel, A. W. & Worster, M. G. 2001 Particle trapping at an advancing solidification front with interfacial-curvature effects. *J. Crystal Growth* **223**, 420–432.

Rogerson, M. A. & Cardoso, S. S. S. 2000 Patterns of bubble desorption during the solidification of a multicomponent melt. *J. Fluid Mech.* **419**, 263–282.

Sasikumar, R. & Ramamohan, T. R. 1991 Distortion of the temperature and solute concentration fields due to the presence of particles at the solidification front—effects on particle pushing. *Acta Metallurgica et Meterialia* **39** (4), 517–522.

Sekhar, J. A. & Trivedi, R. 1991 Solidification microstructure evolution in the presence of inert particles. *Mater. Sci. Engng* A **147**, 9–21.

Sen, S., Kaukler, W. F., Curreri, P. & Stefanescu, D. M. 1997 Dynamics of solid/liquid interface shape evolution near an insoluble particle—an x-ray transmission microscopy investigation. *Metall. Mater. Trans.* A **28** (10), 2129–2135.

Temkin, D. E., Chernov, A. A. & Mel'nikova, A. M. 1977 Capture of foreign particles by a crystal growing from a melt containing impurities. *Soviet Phys.: Crystallogr.* **22** (1), 13–17.

Uhlmann, D. R., Chalmers, B. & Jackson, K. A. 1964 Interaction between particles and a solid-liquid interface. *J. Appl. Phys.* **35**, 2986–2993.

Wang, Z., Mukai, K. & Lee, I. J. 1999 Behavior of fine bubbles in front of the solidifying interface. *ISIJ Intl* **39** (6), 553–562.

Wei, P. S., Huang, C. C. & Lee, K. W. 2003 Nucleation of bubbles on a solidification front-experiment and analysis. *Metall. Mater. Trans.* B **34** (3), 321–332.

Wettlaufer, J. S., Worster, M. G. & Huppert, H. E. 1997 Natural convection during solidification of an alloy from above with application to the evolution of sea ice. *J. Fluid Mech.* **344**, 291–316.

Wilde, G. & Perepezko, J. H. 2000 Experimental study of particle incorporation during dendritic solidification. *Mater. Sci. Engng* A **283** (1–2), 25–37.

Wu, Y., Liu, H. & Lavernia, E. J. 1992 Solidification behavior of Al–Si/SiC MMCs during wedge-mold casting. In *Microstructure Formation During Solidification of Metal Matrix Composites* (ed. P. K. Rohatgi), pp. 41–61. Minerals, Metals & Materials Society.

Yang, Y., Garvin, J. W. & Udaykumar, H. S. 2008 Sharp interface numerical simulation of directional solidification of binary alloy in the presence of a ceramic particle. *Intl J. Heat Mass Transfer* **51** (1–2), 155–168.

Young, N. O., Goldstein, J. S. & Block, M. J. 1959 The motion of bubbles in a vertical temperature gradient. *J. Fluid Mech.* **6**, 350–356.